IEEE Access
Multidisciplinary ⋮ Rapid Review ⋮ Open Access Journal

Received May 13, 2020, accepted May 30, 2020, date of publication June 8, 2020, date of current version June 18, 2020.

Digital Object Identifier 10.1109/ACCESS.2020.3000602

Analysis of Massive MIMO Performance in an Indoor Picocell With High Number of Users

JESÚS R. PÉREZ, RAFAEL P. TORRES, MARTA DOMINGO, LUIS VALLE, AND JOSÉ BASTERRECHEA, (Member, IEEE)
Department of Communications Engineering, Universidad de Cantabria, 39005 Santander, Spain

Corresponding author: Jesús R. Pérez (jesusramon.perez@unican.es)

This work was supported in part by the Spanish Ministerio de Economía, Industria y Competitividad, under Grant TEC2017-86779-C2-1-R, in part by the European economic community (EEC) through Fondo Europeo de Desarrollo Regional (FEDER) funds, and in part by the Spanish Ministerio de Ciencia e Innovación under Grant UCAN08-4E-010.

ABSTRACT This paper presents an analysis of the massive multiple input and multiple output (MIMO) channel in an indoor picocell with a high number of active user terminals and a base station consisting of a virtual array with up to one hundred elements. The analysis is based on the results of a measurement campaign carried out in the 3.2 to 4 GHz band in a scenario of reduced size and with a symmetrical geometry, in which users are also placed in an orderly manner. The channel meets the condition of favorable propagation depending on several factors, one of the most important being the spatial distribution of users. Results concerning the inverse condition number as well as the channel sum capacity are included. Another factor that determines the performance of massive MIMO systems when operated in an orthogonal frequency division multiplexing (OFDM) framework is the frequency selectivity of the channel that limits the size of the coherence block (ChB). Focusing on the most significant results achieved, it can be concluded that the channel reaches a capacity of 89% with respect to an i.i.d. Rayleigh channel. Concerning the cumulative distribution function (CDF) of the sum capacity, it can also be observed that the tails are not very pronounced, which indicates that a homogeneous service can be given to all users. Regarding the number of samples that make up the ChB, although it is high in all cases (of the order of tens of thousands), it strongly depends on the degree of correlation used to calculate the coherence bandwidth.

INDEX TERMS 5G mobile systems, channel capacity, coherence bandwidth, coherence block, massive MIMO.

I. INTRODUCTION

The evolution and subsequent deployment of the fifth generation of mobile communications systems (5G), as well as the development of the next generation (6G) will require the optimum use of the radio channel, enhancing the spectral efficiencies. In addition to the unquestionable need for more spectrum, the deployment of smaller cells and the development of evolved multiple input and multiple output (MIMO) systems are some examples of the representative enabling technologies [1]. Initial MIMO systems were envisaged for point-to-point communications [2], [3]. Later, the concepts of multi-user MIMO were developed [4]–[6], which currently have massive MIMO systems as one of their most promising form [7]–[14].

The performance of a massive MIMO system with respect to the attainable capacity depends largely on the orthogonality between the sub-channels established between the different simultaneously active user terminals (UTs) and the base station (BS) array. For the case of a theoretical channel, known as i.i.d. Rayleigh, it is well established that this orthogonality increases as the number of antenna elements of the array at the BS also grows [8]. In those cases in which this fact occurs we will say that the channel meets the "favorable propagation" condition. Therefore, it is important to know to what extent this condition is verified in real scenarios. In order to carry out such an analysis, massive MIMO channels must be measured in different environments, frequency bands and system configurations, i.e. for arrays with different numbers and types of antennas, as well as for different spatial distributions of the UTs.

From the initial experimental research [15]–[18] to the present, a great deal of work has been performed to empirically characterize massive MIMO channels in different environments and frequency bands. In this sense, a wide

The associate editor coordinating the review of this manuscript and approving it for publication was Zesong Fei.

bibliographic compilation can be found in [19]–[21]. In the case of the characterization of the massive MIMO indoor channels, it is worth highlighting, among others, the recent works [21]–[25]. Unlike existing previous research works, the distinctive feature of the current research is the consideration of a small propagation environment in which up to 20 active UTs are considered. The small size of the cell along with its symmetry, the shortage of furniture and the relative closeness between UTs, form an interesting and realistic environment in which the condition of favorable propagation can be properly tested, as well as the possibility of separating the UTs spatially. From the authors' knowledge, the only work that addresses a similar scenario is the one presented in [26]. The conclusions obtained in our research complement some of those of this previous work, and provide interesting data on another crucial aspect for the proper functioning of massive MIMO systems such as the temporal dispersion of the channel and its impact on the duration of the coherence block (ChB).

In addition to the importance of the favorable propagation condition in the spectral efficiency obtainable from a massive MIMO system, the effective duration of the so-called coherence block is also another aspect of great relevance. The coherence block is defined as the product of the channel's coherence bandwidth (B_C) and the coherence time (T_C). We can say that during this frequency-time block, the channel can be considered flat in frequency and invariant in time and thus, the estimation of the channel is kept up to date. Therefore, the measurement and knowledge of both the B_C and T_C values of the channel is also very important. In this article, the authors present experimental results of the B_C values achieved for the indoor environment considered. The cumulative distribution functions (CDF) of this parameter for several levels of coherence are presented, which provides a statistical estimate of the values that the B_C may reach in such an environment. In addition, results showing the variability of the B_C between the antenna elements of the BS array are presented. Taking into account the influence of the B_C on the duration of the frequency-time coherence block and its role in the time division duplex (TDD) operation framework, knowing its value is crucial for dimensioning current massive MIMO systems operating on the OFDM-TDD basis.

II. CHANNEL MEASUREMENTS

A. ENVIRONMENT

The channel measurements have been carried out in a conference room, equipped with six rows of desks, chairs and two cabinets as the main furniture inside the environment. Moreover, the environment is located in a modern building made of reinforced concrete, with indoor ceiling boards, plasterboard paneled walls as well as metallic doors in all the rooms [27]. Fig. 1 shows a view of the propagation environment which is 8.8 by 14.5 meters in size and the height to the ceiling board is 2.98 m.

FIGURE 1. Front view of the measurement environment.

B. MEASUREMENT SETUP

The channel sounding is carried out using the measurement system shown in Fig. 2, consisting of a planar scanner and the E8362A Keysight Technologies vector network analyzer (VNA), both remote controlled, to measure in the frequency domain the $S_{21}(f)$ scattering parameter, which corresponds with the $H(f)$ or complex channel transfer function (CTF) [27].

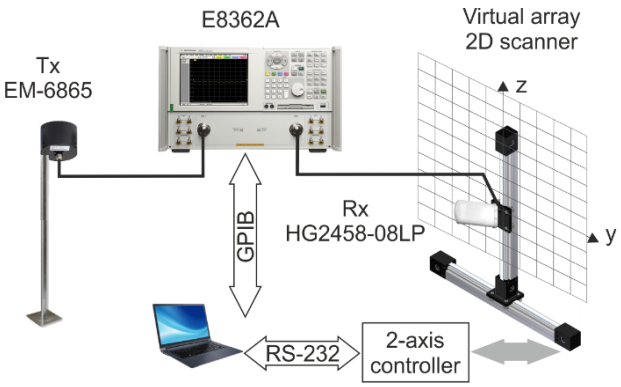

FIGURE 2. Schematic diagram of the channel measurement setup.

The planar scanner consists of two linear units and two associated servomotors and allows the receiver (Rx) antenna to be moved on a vertical plane emulating a virtual array (VA) at the receiver side. At every Rx position of the VA the S_{21}-trace is acquired and, from the post-processing, the CTF as well as a complete characterization of the channel established between the transmitter (Tx), i.e. an active user terminal (UT), and the Rx VA, i.e. the array at the base station (BS), can be accomplished.

Regarding the antennas and noticing that the analysis will be focused on the up-link, a biconical omnidirectional EM-6865 antenna from Electrometrics along with a log-periodic HG2458-08LP antenna from L-Com, both linearly polarized, have been used at Tx and Rx

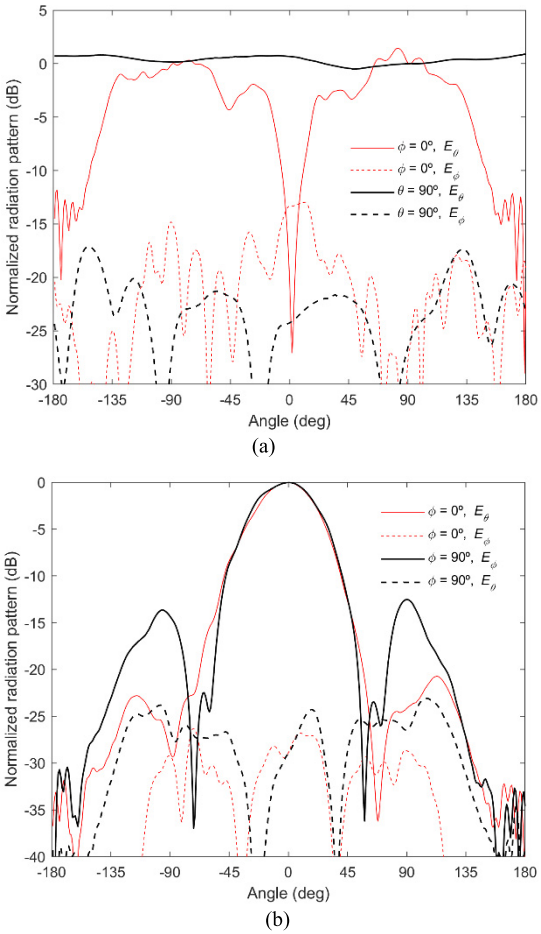

FIGURE 3. Normalized measured radiation patterns cuts at 4 GHz for the antennas considered. (a) EM-6865 antenna. (b) HG2458-08LP antenna.

sides, respectively. The EM-6865 operates in the range 2-18 GHz and the HG2458-08LP in the range 2.3-6.5 GHz. Figure 3 shows the two main cuts of the normalized radiation pattern at 4 GHz measured for both antennas in our anechoic chamber. To carry out the pattern measurements, the biconical antenna was connected to the roll positioner with the same cylindrical metallic rod, 25 cm in length, used to support the antenna during the channel measurements campaign, and centered at the midpoint of the bicone and with its axis aligned with the z-axis of the anechoic chamber measurement system. As can be seen in Figure 3(a), the antenna shows an almost omnidirectional behavior with a ripple of around 1 dB on the horizontal plane ($\theta = 90°$ cut) and crosspolar levels below -15 dB. For the vertical plane ($\phi = 0°$ cut), a ripple of around 1 dB, which is attributed to the combined effect of the metallic supporting rod and the base plate, can be observed and has not been corrected to reproduce the channel measurement configuration in the most realistic way. It has to be taken into account that, for the vertical plane cut, levels for angles higher than $\pm 140°$ must be disregarded due to the blockage effect of the positioner during measurements. Moreover, for the pattern measurements, the log-periodic antenna was centered on the roll over azimuth positioner with the main lobe pointing along the z-axis and the main polarization component aligned with the x-axis. As can be seen in Figure 3(b), the log periodic antenna exhibits a half power beamwidth of approximately 50° on both cuts (E-plane: $\phi = 0°$ cut, H-plane: $\phi = 90°$ cut) and crosspolar levels below -25 dB within the main lobe. In this case, levels for angles further from $\pm 140°$ cannot be taken into account due to the blockage of the roll positioner for both cuts. Gain measurements at 4 GHz provided values of 1.3 and 10.4 dBi for both the biconical and log-periodic antennas, respectively.

C. MEASUREMENT SETTINGS

The $S_{21}(f)$ scattering parameter has been measured in the 3.2 to 4 GHz frequency range, considering for the S_{21}-trace $N_f = 641$ frequency tones $\Delta f = 1.25$ MHz uniformly spaced in the 800 MHz span, i.e. a sampled version of the $H(f)$ or CTF is obtained for any Tx-Rx wireless channel. The frequency resolution considered (Δf) corresponds with a maximum excess delay without aliasing of $1/\Delta f = 800$ ns, leading to a maximum observable distance of 240 m (stated as $c_0/\Delta f$, c_0 being the speed of light), a value far larger than the dimensions of the environment and enough to guarantee that the multipath contributions are properly measured [28]. Further settings of the VNA include a signal level at port 1 of 7 dBm as well as an intermediate frequency (IF) filter bandwidth of 1 kHz as an appropriate trade-off between dynamic range and acquisition time. In this sense, it must be stated that the average signal to noise ratio (SNR) for any of the measurements carried out in this work is above 40 dB. Finally, it should be noted that prior to carrying out the measurement campaign, the VNA has been calibrated at both ends of the radiofrequency cables, so the measured CTF takes into account the joint response of both the channel and the antennas, called in the literature the radio channel [29].

For the measurement campaign and trying to resemble the up-link in a massive MIMO system, the scanner, and thus the Rx directional antenna, has been placed close to the rear wall of the room and with the center of the VA at a height of 2 m. Moreover, the Tx antenna, which would emulate an active UT, has been placed at 20 different positions on the tables of the environment, fixed on a 25 cm rod and at a height of 1.07 m from the floor. For any of the Tx antenna positions considered, the Rx moves on the YZ plane implementing a 10×10 uniform rectangular array (URA) with an inter-element separation in both directions of 50 mm ($\lambda/2$ at 3 GHz or 0.53 λ at 3.2 GHz). This Rx configuration leads to a total scanning area of the URA of 4.8^2 λ^2 at 3.2 GHz. Details of the set of Tx/UT positions considered, all in line-of-sight (LOS) conditions, as well as the location chosen for the Rx/BS is shown in Fig. 4. The Tx-Rx (or UT-BS) distances lie in the range 4.1-11.2 m and a complete measurement for any of the Tx/UT position takes around 17 minutes.

Finally, Table 1 summarizes the main parameters concerning the measurement settings outlined in this subsection.

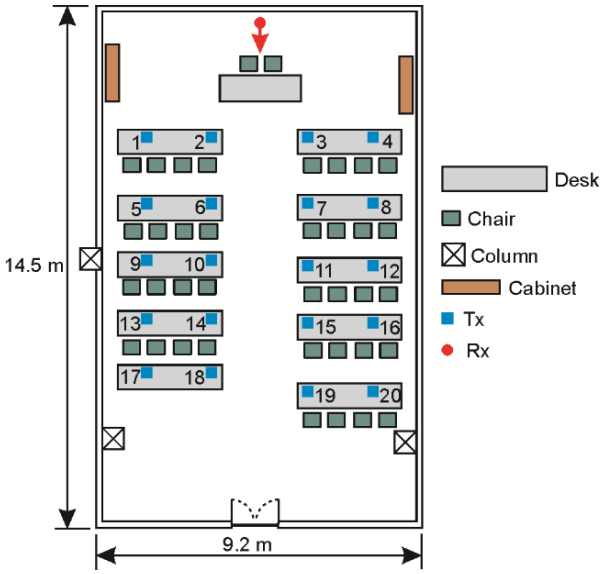

FIGURE 4. Top view of the indoor environment. The arrow shows the Rx antenna broadside direction.

TABLE 1. Representative parameters of the measurement settings.

Frequency Span (GHz)	3.2 – 4.0
Frequency resolution, Δf (MHz)	1.25
Transmission power (dBm)	7
IF bandwidth (kHz)	1
URA, inter-element separation (mm)	50
URA, total scanning area (m^2)	0.2025
Measurement time for a Tx/UT position (min)	17

The analysis of the effect of people on the wireless channel performance is beyond the scope of this research, so it should be noted that all the channel measurements have been carried out at night in order to guarantee stationary conditions.

III. CHANNEL CHARACTERISATION

A. BROADBAND CHANNEL CHARACTERISATION

The channel impulse response can be obtained by applying the inverse discrete Fourier transform to the measured transfer function $H(f)$, i.e. the measured $S_{21}(f)$ for the N_f frequency tones, as shown in (1). Furthermore, this channel transfer function has also been windowed with a Hamming window, W, in order to reduce sidelobe levels.

$$h[n] = \frac{1}{N_f} \sum_{k=0}^{N_f-1} W[k] H[k] exp\left(j\frac{2\pi}{N_f}kn\right) \quad (1)$$

From the channel impulse response, the power delay profile (PDP) is then obtained as $P[n] = |h[n]|^2$ and, from the PDP, some useful magnitudes can be obtained to characterize the channel in the time domain. The root mean square (RMS) delay spread is the statistical parameter obtained from the PDP that best describes the signal dispersion caused by the channel. It is calculated as [29]:

$$\tau_{RMS} = \sqrt{\frac{\sum_{n=1}^{N_f} (\tau_n - \bar{\tau})^2 P[n]}{\sum_{n=1}^{N_f} P[n]}} \quad (2)$$

where τ_n is the n-th excess delay time and $\bar{\tau}$ is given by:

$$\bar{\tau} = \frac{\sum_{n=1}^{N_f} \tau_n P[n]}{\sum_{n=1}^{N_f} P[n]} \quad (3)$$

From the temporal dispersion the channel frequency selectivity can be obtained. For wide-sense stationary uncorrelated scattering channels, the normalized frequency correlation function, denoted by $R_{HH}[l]$, can be obtained by means of the Fourier transform of the PDP [29]:

$$R_{HH}[l] = \frac{\sum_{n=0}^{N_f-1} |h[n]|^2 exp\left(j\frac{2\pi}{N_f}nl\right)}{\sum_{n=0}^{N_f-1} |h[n]|^2} \quad (4)$$

Finally, from the correlation function the coherence bandwidths (B_C) for different correlation levels can be obtained [29].

B. UPLINK MASSIVE MIMO SYSTEM MODEL

Focusing the analysis on the up-link, the massive MIMO system considered is a simple cell system where the BS is equipped with M antennas. The maximum number of active users is Q and each user terminal (UT) is equipped with a single antenna, as depicted in Fig. 5. It is assumed that the users transmit a total power P. In addition, it is assumed that the BS knows the channel and that the UTs are not collaborating among each other. Furthermore, we consider an OFDM system with N_f sub-carriers, which corresponds to the measured tones.

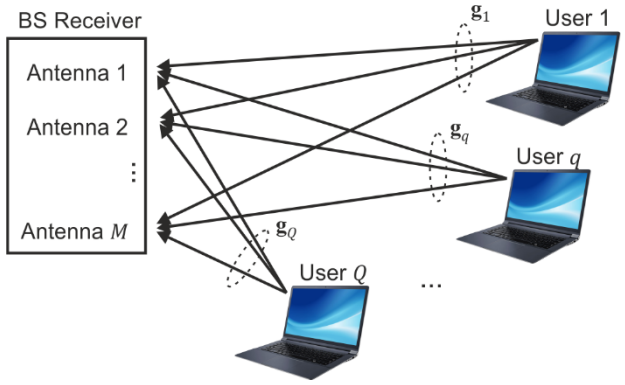

FIGURE 5. Massive MIMO system.

Considering this model, the signal received at the base station for the k-th sub-carrier when the Q users are active will be given by:

$$\mathbf{y}[k] = \sqrt{SNR}\,\mathbf{G}[k] \cdot \mathbf{s}[k] + \mathbf{n}[k]; \quad k = 1, 2, \cdots, N_f \quad (5)$$

where $\mathbf{y}[k]$ is a received signal column vector with M elements corresponding to the k-th sub-carrier; $\mathbf{G}[k]$ is the

channel matrix of order $M \times Q$, in which each one of its columns corresponds with the narrowband channel $g_q[k]$ of order $M \times 1$; $\mathbf{s}[k]$ $(Q \times 1)$ is the signals vector transmitted from the UTs and normalized in such a way that $E\left\{\|\mathbf{s}\|^2\right\} = 1$; and $\mathbf{n}[k]$ is a complex Gaussian noise vector with i.i.d. unit variance elements. Finally, the SNR represents the mean signal to noise ratio at the receiver.

The matrix in (5) is normalized in such a way that verifies:

$$\left\{\|\mathbf{G}\|_F^2\right\} = M \cdot Q \tag{6}$$

Moreover, the matrix $\mathbf{G}$ is obtained from the matrix of the raw channel measurements ($\mathbf{G}^{raw}$) by means of:

$$\mathbf{G}_{M\times Q} = \mathbf{G}^{raw}_{M\times Q}\mathbf{J}_{Q\times Q} \tag{7}$$

The normalization matrix $\mathbf{J}$ is a diagonal matrix of order $Q \times Q$. Different normalizations can be considered, provided they verify (6), which guarantees the conservation of the total transmitted power. Following the proposal and the nomenclature in [11] we consider two normalizations that we will denote as normalization 1 (N1) and normalization 2 (N2).

On the one hand, in case of considering N1, the normalization matrix $\mathbf{J}$ is a diagonal matrix of order $Q \times Q$, whose elements (j_q) are given by

$$j_q = \sqrt{\frac{M}{\frac{1}{N_f}\sum_{k=1}^{N_f}\left|g_q^{raw}[k]\right|^2}}; \quad q = 1, \ldots, Q \tag{8}$$

The elements of the diagonal normalization matrix $\mathbf{J}$ take different values so that all the columns in $\mathbf{G}$ are normalized to one; consequently the power imbalance between the channels corresponding to each UT is eliminated, although the channel variations between antennas within the receiver array and frequency tones are maintained. The resulting normalized matrix, $\mathbf{G}$, can be interpreted as that associated with a system in which an ideal power control is performed. In this case, the total available power transmitted by the users is not distributed equally, but each UT is assigned the necessary power so that all UTs reach the BS with the same mean power.

On the other hand, N2 is defined in such a way that all the elements of the diagonal matrix $\mathbf{J}$ are equal and thus, the operation in (7) is equivalent to multiply the matrix by a scalar:

$$j_q = \sqrt{\frac{MQ}{\frac{1}{N_f}\sum_{k=1}^{N_f}|\mathbf{G}^{raw}[k]|_{\mathrm{F}}^2}}; \quad q = 1, \ldots, Q \tag{9}$$

This normalization keeps the difference between the received power from different UTs, receiver antennas and frequency tones.

Both N1 and N2 normalizations have their pros and cons. The N2 preserves the original structure of the channel and the effect that the power imbalance can have on the system. However, if the aim is to avoid the effect of the power imbalance and exclusively analyse the orthogonality of the channel, for example through the condition number, it is mandatory to use N1 [11].

The spectral efficiency that massive MIMO systems can achieve depends largely on the degree to which the condition of "favorable propagation" is met, which depends on the extent to which the channels of the different users are orthogonal [8]–[12]. A commonly accepted metric used to weigh up the orthogonality of the columns of a matrix is the condition number, κ, which is also a measure of the dispersion of the singular values of the matrix. The condition number of a matrix $\mathbf{G}$ is defined by the relationship:

$$\kappa = \frac{max\left\{eigenvalue\left(\mathbf{G}^H\mathbf{G}\right)\right\}}{min\left\{eigenvalue\left(\mathbf{G}^H\mathbf{G}\right)\right\}} \tag{10}$$

According to (10), a value of κ equal to one corresponds to a channel matrix in which all its columns are orthogonal. Conversely, high values of κ indicate that at least two columns of the matrix will be practically collinear. It is more suitable in order to interpret the results to use the inverse of the condition number (ICN), which varies between 1 (maximum orthogonality) and 0 (zero orthogonality).

To have a direct measure of the goodness of the channel we calculate the sum capacity. Under the hypothesis of a perfect knowledge of the channel at the BS, we can obtain the sum-capacity of the massive MIMO-OFDM system by means of the breakdown into singular values of the channel matrix as

$$C\,(k) = \sum_{q=1}^{Q} log_2\left(1 + \frac{SNR}{Q}\cdot\lambda_q\right); \quad k = 1, 2, \cdots, N_f \tag{11}$$

in which λ_q represents the q-th eigenvalue of the $\mathbf{G}^H\mathbf{G}$ matrix, i.e. the square of the q-th singular value of the $\mathbf{G}$ matrix.

Under favorable propagation conditions, as the number of receiving antennas, M, increases to infinity, and for a fixed number of transmitters Q, the capacity of the up-link channel will tend asymptotically to the upper bound [12]:

$$C_b = Q \cdot log_2\left(1 + \frac{M \cdot SNR}{Q}\right) \tag{12}$$

IV. RESULTS

For the massive MIMO cell presented previously, this section includes the most representative results concerning the temporal dispersion of the channel, its frequency selectivity and the sum capacity. First, both the measured coherence bandwidth and RMS delay spread values are presented and discussed. Secondly, an analysis of the channel sum capacity as a function of system parameters like the SNR or the number of radiating elements at the BS for different number of active users are included.

A. TEMPORAL DISPERSION AND FREQUENCY SELECTIVITY

Wideband communication systems are strongly influenced by the temporal dispersion of the transmitted signals caused by the channel, which is the origin of the frequency selectivity. As outlined in the previous section, channel parameters such

as the mean delay and the RMS delay spread can be directly obtained from the PDP, and the coherence bandwidth at different levels of correlation, which quantifies the frequency selectivity of the channel, depends also on the PDP. In this subsection, results involving these parameters are presented and discussed.

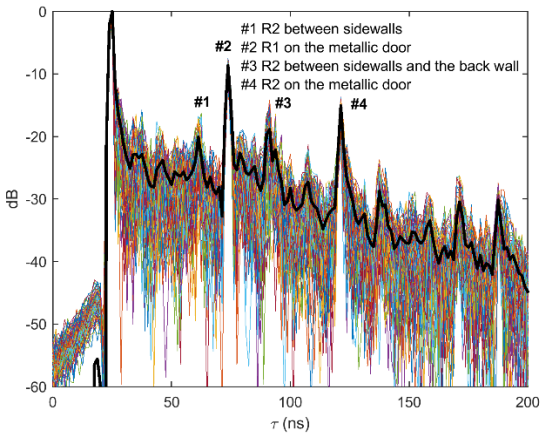

FIGURE 6. Representative PDP considering UT_{10} and showing details of the some relevant contributions of the multipath. R1 and R2 stands for first and second order reflections.

In Fig. 6, we present the PDPs corresponding to the100 channels established between UT_{10} and the 100 antennas at the BS. The results shown are representative of what happens as a general trend for the rest of the measured UT positions. The black line represents the average PDP. An important variability is observed in the received power values for different delay times, especially on the interval between 20 and 60 ns, in which the variability margin reaches $+/-$ 6 dB with respect to the average value. This variability will be present in the values of the RMS delay spread and B_C obtained. The contributions in this time interval correspond mainly with first and higher order reflections in the environment close to the BS. Furthermore, the average PDP presents a series of maxima or peaks to which all the antennas contribute almost simultaneously and which correspond to reflections from larger and more distant reflectors. In Fig. 6, the maximum #1 is due to double reflections (R2) between the sidewalls; #2 is caused by a very strong reflection (R1) on the metallic door on the back wall of the room. The peak #3 originates from R2 between the sidewalls and the back wall; and finally the maximum #4 is due to R2 on the metallic door of the room.

Fig. 7 shows the RMS delay spread values obtained for each UT along the antenna elements that make up the array. The top and bottom of each box represent the 25% and 75% percentiles of the samples, respectively; and thus, the distance between both top and bottom of the box represents the interquartile range. Whiskers are drawn from the ends of the interquartile ranges to the furthest observations. A great dispersion of the RMS delay spread values achieved is observed for most of the UT positions

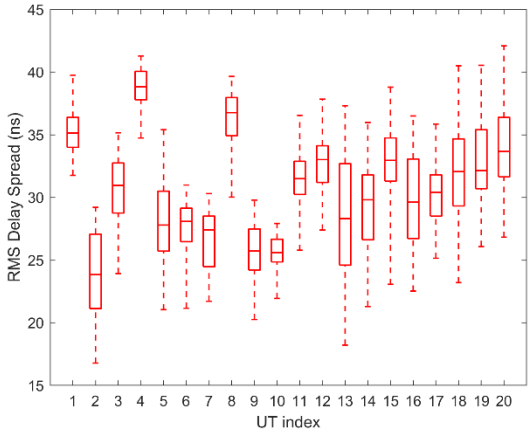

FIGURE 7. RMS delay spread values for the whole scenario.

investigated. No dependence with the position of the UTs or on the distances between them and the BS is appreciated.

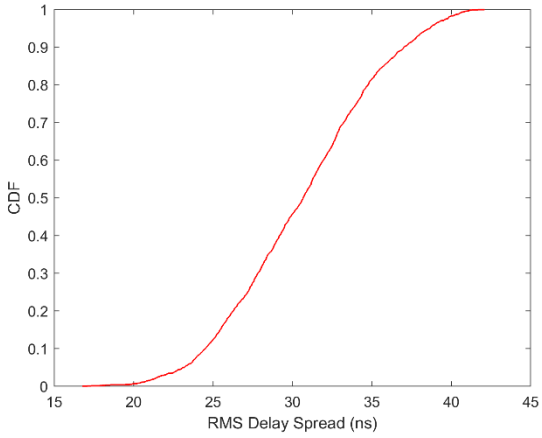

FIGURE 8. CDF of the RMS delay spread.

The associated CDF of the RMS delay spread for all the UTs is shown in Fig. 8. It takes values between approximately 17 and 43 ns, which agrees with the values reported in [27] in which values lie within the range of 18 and 35 ns for a similar indoor environment and measurement frequency band.

Fig. 9 shows the B_C values obtained for 50%, 70% and 90% of correlation levels. In accordance with the values of the RMS delay spread obtained, a significant dispersion of the B_C values is observed for most UTs, and this dispersion decreases as the degree of coherence increases.

Fig. 10 shows the CDF of the coherence bandwidth for the three levels of correlation considered, and the most significant values of B_C for the three correlation levels are summarized in Table 2.

The minimum coherence bandwidth values range from 1.7 to 4.8 MHz, whereas the maximum values obtained lie in the range of 44.1 to 286.1 MHz. Moreover, the median values range from 2.5 to 117.5 MHz, and the 10% outage B_C values range from 2.0 to 7.6 MHz for the 90 and 50% correlation level cases, respectively. A significant effect is the convergence of the CDF at the lower end of the curves in such a way that the 10% outage coherence bandwidth values are

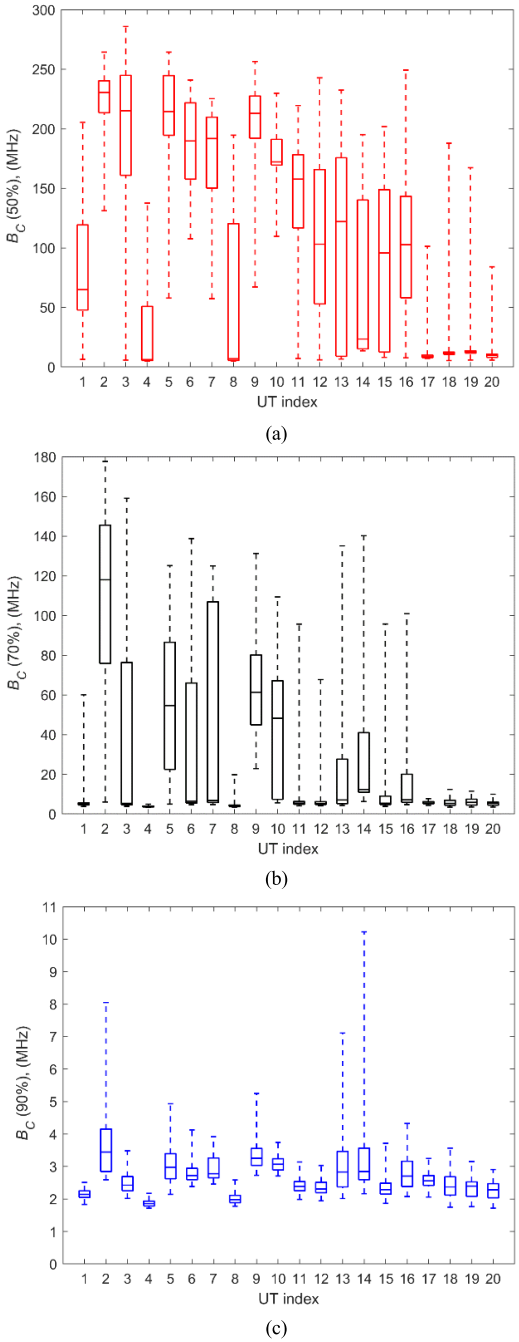

FIGURE 9. Coherence bandwidth for different correlation levels. (a) 50%. (b) 70%. (c) 90%.

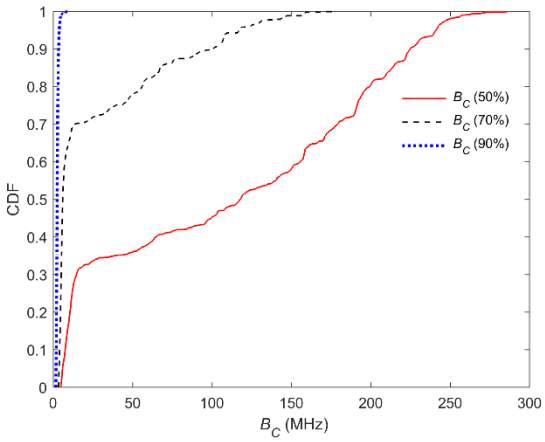

FIGURE 10. CDF of the coherence bandwidth for different correlation levels.

TABLE 2. Significant values of coherence bandwidth for different correlation levels. Values in MHz.

C. level (%)	B_C (min)	B_C (max)	B_C (median)	B_C (10%)
50	4.8	286.1	117.5	7.6
70	3.3	177.6	6.2	4.1
90	1.7	44.1	2.5	2.0

If we make a rough estimate of the T_C following the Clarke model [29], [30], then the coherence time of the channel at a correlation level of 70% can be obtained from the expression:

$$T_C = \frac{9\lambda}{16\pi v} \tag{13}$$

If we consider a typical indoor speed of $v = 0.75$ m/s (2.7 km/h) we obtain a T_C value of approximately 20 ms at the central frequency (3.6 GHz). Thus, considering the B_C values shown in Table 2, we obtain the N_C values summarized in Table 3.

TABLE 3. Number of samples of the coherence block, N_C. Values $\times 10^3$.

Correlation level (%)	N_C (min)	N_C (max)	N_C (median)	N_C (10%)
50	96	5722	2350	152
70	66	3552	124	82
90	34	882	50	40

of the same order of magnitudes for all the three correlation levels with an approximate ratio of two between them.

In massive MIMO networks operated in an OFDM framework, the duration of the ChB is the key when determining the overhead due to channel estimation. A coherence block consists of the number of subcarriers and time samples over which the channel response can be approximated as constant in time and flat fading in frequency. If the coherence bandwidth is B_C and the coherence time is T_C, then each ChB contains $N_C = B_C T_C$ samples.

The results in Table 3 show remarkable differences between the ChB samples depending on the correlation level. Therefore, it is important to determine which degree of correlation should be required to consider the channel effectively flat fading during B_C. Likewise, the dispersion of the N_C values shows the convenience of having more experimental data, not only of B_C values, but also of T_C. This is especially relevant for outdoor channels with high mobility, where N_C can decrease by several orders of magnitude, reaching values of only a few hundred samples.

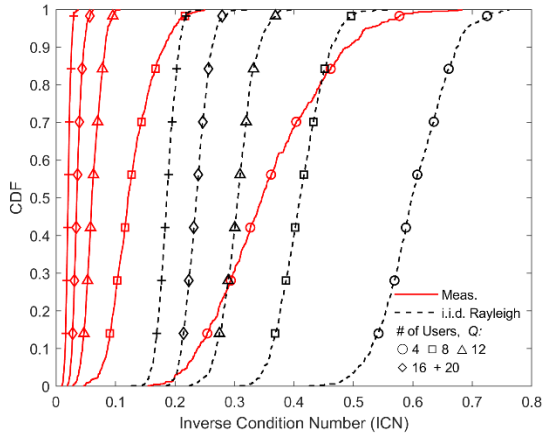

FIGURE 11. CDF of the inverse condition number.

B. INVERSE CONDITION NUMBER AND SUM CAPACITY

Fig. 11 shows the CDF of the inverse condition number (ICN) for this environment as well as for the i.i.d. Rayleigh channels for different number of active UTs, Q, ranging from 4 to 20. In all cases the ICN reached is far below the i.i.d. Rayleigh cases. This means that, as might be expected, there is a loss of orthogonality with respect to the theoretical uncorrelated channels. The loss of orthogonality of the channels can also be observed when the number of users, Q, increases.

Fig. 12(a) presents the CDF of the sum capacity for the environment when N1 is considered, along with the i.i.d. Rayleigh channel cases for a SNR of 10 dB and for different number of active UTs, Q, ranging from 4 to 20. Once again, the results show how the measured capacities are lower than the ones corresponding to the i.i.d. channels. Mean capacities decrease with respect to the i.i.d. Rayleigh channels case as the number of UTs increases. However, in the most unfavorable case of having 20 active UTs, a medium value capacity of 89% of the i.i.d. Rayleigh channel is achieved. In Fig. 12(b), a comparison between the sum capacity CDFs obtained when using both N1 and N2 normalizations is presented. As already found in [25], the capacity obtained using N1, i.e. compensating for the power imbalance between users, is greater than when it is maintained. In this sense, it can be concluded that a power control is adequate, especially when the number of active users increases. Moreover, it is important to note that in both cases the tails of the CDFs are not very pronounced, which indicates that a homogeneous service can be given to all UTs.

Fig. 13 shows the mean capacity as a function of the SNR for different number of UTs, ranging from 4 to 20. Moreover, the figure also shows the associated i.i.d. Rayleigh channel cases. It can be clearly observed the increased loss of capacity with respect to the Rayleigh channel cases as Q increases. This loss remains almost constant for SNR values higher than around 5 dB.

Finally, Fig. 14 shows the mean value of the capacity for different number of UTs as the number of antennas at the BS site increases from 25 to 100. The i.i.d. Rayleigh channel

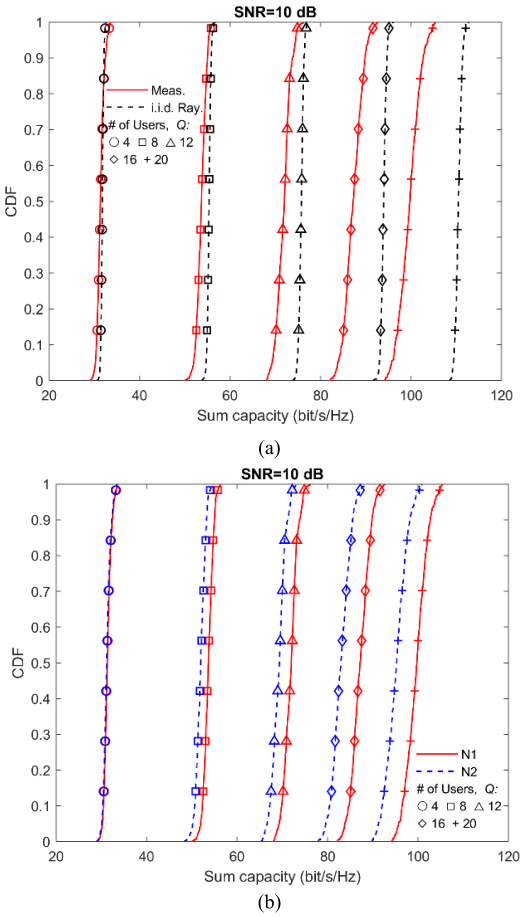

FIGURE 12. CDF of the sum capacity.(a) Comparison with the i.i.d. Rayleigh channel. (b) Comparison between the current normalization (N1) and a global one (N2).

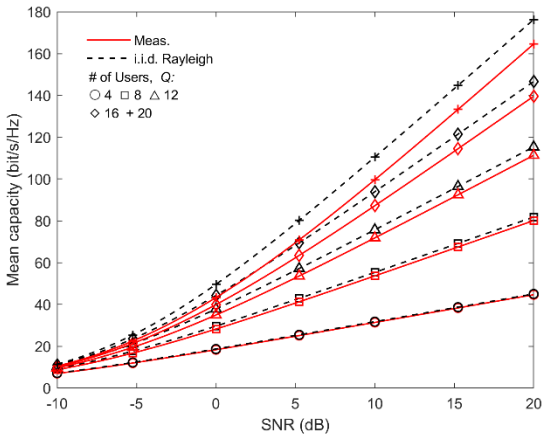

FIGURE 13. Mean capacity of the system against the SNR.

cases are also included as well as the asymptotic value of 113.5 bit/s/Hz for $Q = 20$ users and $M = 100$ antennas. An increase of capacity with the number of antennas at the BS can be observed. However, the measured capacities remain below the values obtained for the theoretical channels, with losses of the order of 10 bit/s/Hz for $Q = 20$. It is also observed that the slope of the mean capacity curve versus the

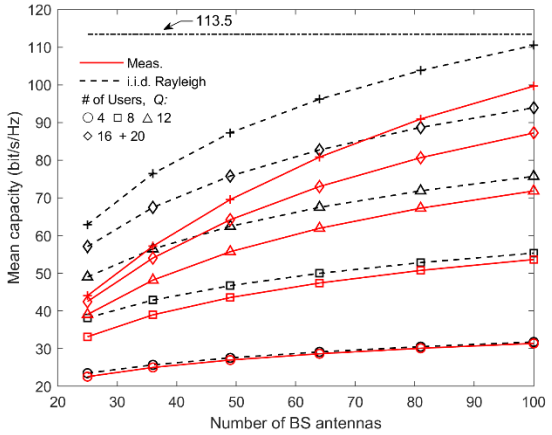

FIGURE 14. **Mean capacity of the system against the number of antennas considered at the base station (BS).**

number of antennas at the BS reaches that of the reference channels when the M/Q ratio is approximately 4.

V. CONCLUSION

The aim of this research focuses on the experimental analysis of a massive MIMO channel in an indoor picocell, considering a high number of active users. The measurements carried out emulate a realistic environment in which a BS, with up to 100 antenna elements making up the virtual array, covers a medium-sized meeting room in which the users are sitting down and the active devices can resemble either laptops or mobile phones at the tables. In addition, the room is very poorly furnished and the resulting configuration is of high symmetry. Therefore, it is an interesting situation to assess to what extent the "favorable propagation" condition is satisfied, and to evaluate the expected values of the B_C achieved.

Focusing on the results achieved and regarding the temporal dispersion of the channel, a great variability of the values of the mean square delay, and consequently of the coherence bandwidth can be observed. The coherence bandwidths obtained show very scattered values, not only among different UTs, but also for the M sub-channels established between a specific UT and the BS. The CDF of the B_C obtained for the three correlation values considered present a significant convergence in the lower tail of the CDF, so the 10% outage B_C values achieved are of the same order of magnitude for the all three correlation levels. However, the 10% outage B_C values practically double when the correlation level falls from 90% (2.0 MHz) to 70% (4.1 MHz) and 50% (7.6 MHz). This fact is of great importance in the definition of the coherence block in the systems operated in the MU-MIMO-OFDM scheme. The results show remarkable differences between the ChB samples depending on the correlation level. Therefore, it is important to determine which degree of correlation should be required to consider the channel effectively flat fading during B_C. Likewise, the dispersion of the N_C values shows the convenience of having more experimental data, not only of B_C values, but also of T_C. This is especially relevant for outdoor channels with high mobility, in which N_C can decrease by several orders of magnitude, reaching values of only a few hundred samples.

The ICN values show that the massive MIMO channel presents a loss of orthogonality with respect to the reference i.i.d. Rayleigh channel. This loss of orthogonality is also reflected in the sum capacity. However, high capacity values are obtained, i.e. in the case of 20 active UTs, the channel reaches a capacity of 89% with respect to an i.i.d Rayleigh channel, which for a SNR of 10 dB is 98.7 bits/s/Hz. It is also observed that the slope of the mean capacity curve versus the number of antennas at the BS reaches the level of that of the reference channels for a ratio $M/Q = 4$. Concerning the CDF of the sum capacity, it can also be observed that the tails are not very pronounced, which indicates that a homogeneous service can be given to all UTs. Consequently, it can be affirmed that the massive MIMO channel analyzed allows users to be spatially separated despite their high number and proximity.

REFERENCES

[1] *IMT Vision—Framework and Overall Objectives of the Future Development of IMT for 2020 and Beyond*, document Recommendation ITU-R M.2083-0, 2015.
[2] G. J. Foschini and M. J. Gans, "On Limits of wireless communications in a fading environment when using multiple antennas," *Wireless Pers. Commun.*, vol. 6, no. 3, pp. 311–335, 1998, doi: 10.1023/A:1008889222784.
[3] E. Telatar, "Capacity of multi-antenna Gaussian channels," *Eur. Trans. Telecommun.*, vol. 10, no. 6, pp. 585–595, Nov. 1999.
[4] G. Caire and S. Shamai, "On the achievable throughput of a multiantenna Gaussian broadcast channel," *IEEE Trans. Inf. Theory*, vol. 49, no. 7, pp. 1691–1706, Jul. 2003, doi: 10.1109/TIT.2003.813523.
[5] S. Vishwanath, N. Jindal, and A. Goldsmith, "Duality, achievable rates, sum-rate capacity of Gaussian MIMO broadcast channels," *IEEE Trans. Inf. Theory*, vol. 49, no. 10, pp. 2658–2668, Oct. 2003, doi: 10.1109/TIT.2003.817421.
[6] D. Gesbert, M. Kountouris, R. W. Heath, C.-B. Chae, and T. Salzer, "Shifting the MIMO paradigm," *IEEE Signal Process. Mag.*, vol. 24, no. 5, pp. 36–46, Sep. 2007, doi: 10.1109/MSP.2007.904815.
[7] T. L. Marzetta, "How much training is required for multiuser MIMO?" in *Proc. Fortieth Asilomar Conf. Signals, Syst. Comput.*, 2006, pp. 359–363.
[8] T. L. Marzetta, "Noncooperative cellular wireless with unlimited numbers of base station antennas," *IEEE Trans. Wireless Commun.*, vol. 9, no. 11, pp. 3590–3600, Nov. 2010, doi: 10.1109/TWC.2010.092810.091092.
[9] E. Björnson, E. G. Larsson, and T. L. Marzetta, "Massive MIMO: Ten myths and one critical question," *IEEE Commun. Mag.*, vol. 54, no. 2, pp. 114–123, Feb. 2016.
[10] T. E. Bogale and L. B. Le, "Massive MIMO and mmWave for 5G wireless HetNet: Potential benefits and challenges," *IEEE Veh. Technol. Mag.*, vol. 11, no. 1, pp. 64–75, Mar. 2016, doi: 10.1109/MVT.2015.2496240.
[11] X. Gao, O. Edfors, F. Rusek, and F. Tufvesson, "Massive MIMO performance evaluation based on measured propagation data," *IEEE Trans. Wireless Commun.*, vol. 14, no. 7, pp. 3899–3911, Jul. 2015, doi: 10.1109/TWC.2015.2414413.
[12] F. Rusek, D. Persson, B. Kiong Lau, E. G. Larsson, T. L. Marzetta, and F. Tufvesson, "Scaling up MIMO: Opportunities and challenges with very large arrays," *IEEE Signal Process. Mag.*, vol. 30, no. 1, pp. 40–60, Jan. 2013, doi: 10.1109/MSP.2011.2178495.
[13] E. G. Larsson, O. Edfors, F. Tufvesson, and T. L. Marzetta, "Massive MIMO for next generation wireless systems," *IEEE Commun. Mag.*, vol. 52, no. 2, pp. 186–195, Feb. 2014, doi: 10.1109/MCOM.2014.6736761.
[14] H. Quoc Ngo, E. G. Larsson, and T. L. Marzetta, "Energy and spectral efficiency of very large multiuser MIMO systems," *IEEE Trans. Commun.*, vol. 61, no. 4, pp. 1436–1449, Apr. 2013, doi: 10.1109/TCOMM.2013.020413.110848.

[15] S. Payami and F. Tufvesson, "Channel measurements and analysis for very large array systems at 2.6 GHz," in *Proc. 6th Eur. Conf. Antennas Propag. (EUCAP)*, Mar. 2012, pp. 433–437.
[16] J. Hoydis, C. Hoek, T. Wild, and S. ten Brink, "Channel measurements for large antenna arrays," in *Proc. Int. Symp. Wireless Commun. Syst. (ISWCS)*, Aug. 2012, pp. 811–815.
[17] J. Li and Y. Zhao, "Channel characterization and modeling for large-scale antenna systems," in *Proc. 14th Int. Symp. Commun. Inf. Technol. (ISCIT)*, Sep. 2014, pp. 559–563.
[18] B. Zhang, Z. Zhong, B. Ai, R. He, F. Tufvesson, J. Flordelis, Q. Wang, and J. Li, "Empirical evaluation of indoor multi-user MIMO channels with linear and planar large antenna arrays," in *Proc. IEEE 28th Annu. Int. Symp. Pers., Indoor, Mobile Radio Commun. (PIMRC)*, Oct. 2017, pp. 1–6.
[19] J. Zhang, M. Shafi, A. F. Molisch, F. Tufvesson, S. Wu, and K. Kitao, "Channel models and measurements for 5G," *IEEE Commun. Mag.*, vol. 56, no. 12, pp. 12–13, Dec. 2018, doi: 10.1109/MCOM.2018.8570033.
[20] Z. Lin, X. Du, H.-H. Chen, B. Ai, Z. Chen, and D. Wu, "Millimeter-wave propagation modeling and measurements for 5G mobile networks," *IEEE Wireless Commun.*, vol. 26, no. 1, pp. 72–77, Feb. 2019, doi: 10.1109/MWC.2019.1800035.
[21] F. Challita, P. Laly, M. Liénard, E. Tanghe, W. Joseph, and D. P. Gaillot, "Hybrid virtual polarimetric massive MIMO measurements at 1.35 GHz," *IET Microw., Antennas Propag.*, vol. 13, no. 15, pp. 2610–2618, Dec. 2019, doi: 10.1049/iet-map.2018.6120.
[22] F. Challita, M.-T. Martinez-Ingles, M. Lienard, J.-M. Molina-Garcia-Pardo, and D. P. Gaillot, "Line-of-Sight massive MIMO channel characteristics in an indoor scenario at 94 GHz," *IEEE Access*, vol. 6, pp. 62361–62370, 2018, doi: 10.1109/ACCESS.2018.2876225.
[23] A. O. Martinez, J. O. Nielsen, E. De Carvalho, and P. Popovski, "An experimental study of massive MIMO properties in 5G scenarios," *IEEE Trans. Antennas Propag.*, vol. 66, no. 12, pp. 7206–7215, Dec. 2018, doi: 10.1109/TAP.2018.2871881.
[24] E. L. Bengtsson, F. Rusek, P. C. Karlsson, F. Tufvesson, and O. Edfors, "Simulation of multiple-antenna terminal performance in massive MIMO systems based on indoor measurements," *IEEE Trans. Veh. Technol.*, vol. 69, no. 1, pp. 418–427, Jan. 2020, doi: 10.1109/TVT.2019.2949738.
[25] J. R. Perez and R. P. Torres, "On the impact of the radiation pattern of the antenna element on MU-MIMO indoor channels," *IEEE Access*, vol. 8, pp. 25459–25467, 2020, doi: 10.1109/ACCESS.2020.2970769.
[26] J. Flordelis, F. Rusek, X. Gao, G. Dahman, O. Edfors, and F. Tufvesson, "Spatial separation of closely-located users in measured massive MIMO channels," *IEEE Access*, vol. 6, pp. 40253–40266, 2018, doi: 10.1109/ACCESS.2018.2854307.
[27] J. R. Perez, R. P. Torres, L. Rubio, J. Basterrechea, M. Domingo, V. M. R. Penarrocha, and J. Reig, "Empirical characterization of the indoor radio channel for array antenna systems in the 3 to 4 GHz frequency band," *IEEE Access*, vol. 7, pp. 94725–94736, 2019, doi: 10.1109/ACCESS.2019.2928421.
[28] L. Rubio, R. P. Torres, V. M. Rodrigo, J. R. Pérez, H. Fernández, J. M. Molina, and J. Reig, "Contribution to the channel path loss and time-dispersion characterization in an office environment at 26 GHz," *Electronics*, vol. 8, no. 11, 1261, pp. 1–14, Nov. 2019, doi: 10.3390/electronics8111261.
[29] J. D. Parsons, "Wideband channel characterization," in *The Mobile Radio Propagation Channel*, 2nd ed. Hoboken, NJ, USA: Wiley, 2000, ch. 6, pp. 164–189.
[30] R. Steele and L. Hanzo, "Mobile radio channels," in *Mobile Radio Communications*, 2nd ed. Chichester, U.K.: Wiley, 1999, ch. 2, pp. 91–118.

JESÚS R. PÉREZ received the B.Sc., M.Sc., and Ph.D. degrees in telecommunications engineering from the Universidad de Cantabria, Spain, in 1996, 1999, and 2005, respectively. He joined the Department of Communications Engineering, Universidad de Cantabria, in 1999, and he was awarded a graduate research and a postdoctoral grant, in 2002 and 2006, respectively. He became an Associate Professor, in 2009. His research interests include computational electromagnetics, optimization methods, antenna measurement techniques, radio propagation, and measurement techniques for the experimental characterization of the radio channel.

RAFAEL P. TORRES received the M.S. degree in physics from Granada University, Spain, in 1986, and the Ph.D. degree in telecommunications engineering from the Polytechnic University of Madrid (UPM), in 1990. He became an Associate Professor with the Department of Communications Engineering, Universidad de Cantabria, Spain, where he is currently a Full Professor in signal processing and communications engineering. His fundamental lines of research have been in the development of numerical methods for the analysis and design of antennas, the applications of high-frequency techniques for simulation, and the analysis of the radar section, as well as the design of radar systems. Since the 1990s, his research has been focusing on the study, modeling, and measurement of the radio channel, and the analysis of its impact on mobile and wireless communications systems. His main achievements focus on the development of ray-tracing methods to simulate the radio channel in complex propagation environments, the experimental characterization of the channel, both SISO and MIMO, and the development of space-time coding techniques.

MARTA DOMINGO received the M.Sc. and Ph.D. degrees in physics (electronics) from the Universidad de Cantabria, in 1989 and 1994, respectively. She became an Associate Professor with the Department of Communication Engineering, Universidad de Cantabria. She was involved in several research projects, and she has authored several articles and conference papers. Her research interests include numerical and high-frequency methods, simulation and measurement techniques for radio propagation, and channel characterization for wireless and mobile communications.

LUIS VALLE received the M.Sc. and Ph.D. degrees in physics (electronics) from the Universidad de Cantabria, Spain, in 1990 and 1996, respectively. He became an Associate Professor with the Department of Communication Engineering, Universidad de Cantabria. He has authored several articles and conference papers. His research interests include numerical and high-frequency methods in electromagnetics applied to antennas and microwave components, radio propagation, and mobile communications.

JOSÉ BASTERRECHEA (Member, IEEE) received the M.Sc. and Ph.D. degrees in physics (electronics) from the Universidad de Cantabria, in 1987 and 1992, respectively. He joined the former Department of Electronics, Universidad de Cantabria, in 1987, and he was a National Graduate Research Fellow, from 1988 to 1991. He became an Assistant Professor with the Department of Communications Engineering, in 1992, and he earned an Associate Professor position, in 1995. His research interests include numerical methods, electromagnetic compatibility, antenna measurement techniques, and optimization and synthesis methods.